

High-efficiency quantum Monte Carlo algorithm for extracting entanglement entropy in interacting fermion systems

Weilun Jiang,^{1,2} Gaopei Pan,^{3,*} Zhe Wang,^{4,5} Bin-Bin Mao,⁶ Heng Shen,^{1,2,†} and Zheng Yan^{4,5,‡}

¹*State Key Laboratory of Quantum Optics and Quantum Optics Devices,
Institute of Opto-Electronics, Shanxi University, Taiyuan, 030006, China*

²*Collaborative Innovation Center of Extreme Optics, Shanxi University, Taiyuan, 030006, China*

³*Institut für Theoretische Physik und Astrophysik and Würzburg-Dresden Cluster
of Excellence ct.qmat, Universität Würzburg, 97074 Würzburg, Germany*

⁴*Department of Physics, School of Science and Research Center for Industries of the Future, Westlake University, Hangzhou 310030, China*

⁵*Institute of Natural Sciences, Westlake Institute for Advanced Study, Hangzhou 310024, China*

⁶*School of Foundational Education, University of Health and Rehabilitation Sciences, Qingdao 266000, China*

(Dated: October 1, 2024)

The entanglement entropy probing novel phases and phase transitions numerically via quantum Monte Carlo has made great achievements in large-scale interacting spin/boson systems. In contrast, the numerical exploration in interacting fermion systems is rare, even though fermion systems attract more attentions in condensed matter. The fundamental restriction is that the computational cost of fermion quantum Monte Carlo ($\sim \beta N^3$) is much higher than that of spin/boson ($\sim \beta N$). To tackle the problem cumbersome existent methods of entanglement entropy calculation, we propose a fermionic quantum Monte Carlo algorithm based on the incremental technique along physical parameters, which greatly improves the efficiency of extracting entanglement entropy. Taking a two-dimensional square lattice Hubbard model as an example, we demonstrate the effectiveness of the algorithm and show the high computation precision. In this simulation, the calculated scaling behavior of the entanglement entropy elucidates the different phases of the Fermi surface and Goldstone modes.

Introduction.— Quantum entanglement, a key non-classical resource in quantum information processing, recently has been discovered that may also be one of the fundamental mechanisms of condensed matter physics [1–4]. In practice, the entanglement entropy (EE) is generally used as a measure of quantum entanglement, especially in many-body physics. While quantum field theory and conformal field theory have difficulties in complex systems or near certain quantum criticalities [5–17], numerical methods offer a universal approach to calculate EE, revealing intrinsic properties beyond local operators, such as the information from conformal field theory, topological order, and Goldstone modes [8, 18–20]. Recent decade has witnessed significant progress in developing efficient algorithms for large-scale, high-dimensional interacting systems [21–44].

Among these, the quantum Monte Carlo (QMC) method is by far one of the most promising algorithms for large-scale sign-free systems in two and higher dimensions. It is not limited to specific forms of EE, no matter area law or volume law, and is an unbiased algorithm. Although the QMC algorithms of spin/boson systems with an $O(\beta N)$ complexity have been widely leveraged to obtain entanglement information in various phases and phase transition points [21–25, 45–51], the QMC algorithms of EE in fermion systems are few because of the algorithmic structure with $O(\beta N^3)$ complexity for fermionic calculations, where N is the total number of sites and β is the inverse temperature or projection length. Therefore, for a long time, research on the entanglement entropy of fermionic systems grows slowly. However, the main topic of condensed matter are the emergent phenomena in interacting-electron systems, such as high-temperature superconductivity, quantum Hall effect, and twisted bilayer materi-

als, all of which are fermionic. How to extract the entanglement properties of these fermion systems is an important but challenging issue.

The pioneering QMC work for calculating EE in fermionic systems was proposed by Grover, which is based on determinantal QMC (DQMC) [23], later extended to projection QMC (PQMC) [52, 53]. Despite this method is theoretically rigorous, it becomes cumbersome when dealing with situations far from the free fermion limit. Specifically, the distribution of its observables tends to be broad, leading to a non-importance sampling, which in turn causes the average value of the EE to converge slowly. To address the issue of convergence and improve the computation precision, the incremental technique maturely used in bosonic QMC [21, 45, 52, 54] has been generalized to fermionic QMC [32, 53, 55–57]. The key spirit is smoothly connecting two far-away distributions by inserting several intermediate distributions, thereby the importance sampling can be realized. Here the two far-away distributions mean the distributions of the partition function and of the targeted observable.

Although the incremental technique has highly improved the precision of the EE data measured by QMC, the virtually introduced intermediate-processes largely increase the computational cost. Usually, the number of intermediate processes needs to be kept as an algebraic growth with system length L , then the importance sampling can be held [56, 58]. To enable the EE to be universally applied in the study of interacting-fermion systems, the improvement of computational efficiency of fermion QMC is highly demanded. Here, in order to fix this problem we develop a fermionic QMC algorithm for calculating the EE with high-efficiency and low-computational-cost.

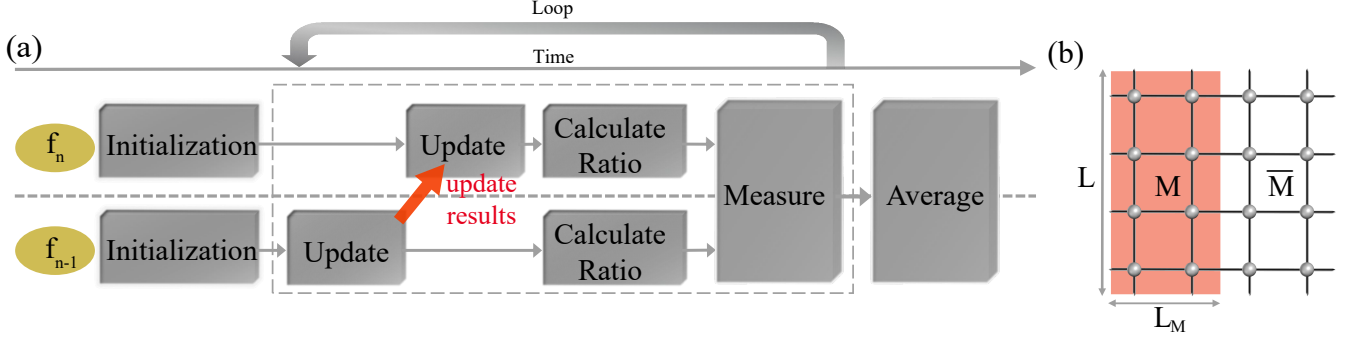


FIG. 1. Overview of the algorithm. (a) Algorithm flow diagram for calculating $\mathcal{Z}(f_n)/\mathcal{Z}(f_{n-1})$. The upper and lower part separated by the dashed line represents two identical memory space for two parameter sets f_n and f_{n-1} , respectively. Note the update results are the update sequence of lattice points and whether these updates occur, according to the ratio of f_{n-1} . (b) Sketch map for the square lattice with length L and period boundary condition. The rectangle entangled subregion is colored by red with $L_M \times L_M$, where $L_M = L/2$.

Method.— We take PQMC as an example to illustrate the mechanism of our algorithm. In fact, this method can be also implemented in DQMC generally with same spirit [59, 60]. As routinely doing in QMC simulation, we consider the calculation of second Rényi EE $S_M^{(2)}$ defined on the subregion M (\bar{M} is the environment) for general interacting fermions. Accordingly, $S_M^{(2)} = -\ln \text{Tr} \rho_M^2$, where ρ_M is the reduced density matrix of subregion M . In PQMC regime, $S_M^{(2)}$ can be formularized as the ratio of two partition functions,

$$S_M^{(2)} = -\ln \frac{Z_M^{(2)}}{Z^2}, \quad (1)$$

where $Z_M^{(2)} = \sum_{s_1, s_2} W_{s_1} W_{s_2} \det g_{M, s_1, s_2}$, $Z = \sum_{s_1} W_{s_1}$ with the auxiliary fields labeled s_1 and s_2 [61]. $g_{M, s_1, s_2} = G_{M, s_1} G_{M, s_2} + (\mathbb{1} - G_{M, s_1})(\mathbb{1} - G_{M, s_2})$ is referred to as the Grover matrix, which is decided by the Green function matrix G for both s_1, s_2 [23]. W_{s_1} represents the standard configuration weight of s_1 in QMC.

In the beginning, all the methods aim to directly calculate the overlap between $Z_M^{(2)}$ and Z^2 to obtain the EE by Eq.(1). Though being theoretically rigorous, the overlap is exponentially small as the system size increases, resulting in a poor sampling efficiency. To overcome this difficulty, the incremental technique has been introduced by dividing the small value of the overlap into the product of several larger values [25, 31, 53, 55, 62]. A typical manner is to transform the ratio $\frac{Z_M^{(2)}}{Z^2} = \frac{\sum_{s_1, s_2} W_{s_1} W_{s_2} \det g_{M, s_1, s_2}}{\sum_{s_1, s_2} W_{s_1} W_{s_2}}$ into $\frac{\sum_{s_1, s_2} W_{s_1} W_{s_2} (\det g_{M, s_1, s_2})^\delta}{\sum_{s_1, s_2} W_{s_1} W_{s_2}} \times \frac{\sum_{s_1, s_2} W_{s_1} W_{s_2} (\det g_{M, s_1, s_2})^{2\delta}}{\sum_{s_1, s_2} W_{s_1} W_{s_2} (\det g_{M, s_1, s_2})^\delta} \times \dots \times \frac{\sum_{s_1, s_2} W_{s_1} W_{s_2} (\det g_{M, s_1, s_2})^{n\delta}}{\sum_{s_1, s_2} W_{s_1} W_{s_2} (\det g_{M, s_1, s_2})^{(n-1)\delta}}$, where $\delta = 1/n$ and n is a large number to ensure each divided ratio is not too small. In this way, the precision of EE has been improved. However, the intermediate ratios in present methods are unmeaning and consume a lot of computational resources.

Instead, a simpler way is to estimate the EE value at a certain parameter point from that at its nearby point, that is, the

spirit of “reweight”. The ratio of two close partition functions \mathcal{Z} can be measured through the averaged ratio between two related weights [58],

$$\frac{\mathcal{Z}(f_n)}{\mathcal{Z}(f_{n-1})} = \left\langle \frac{\mathcal{W}_{s_1, s_2}(f_n)}{\mathcal{W}_{s_1, s_2}(f_{n-1})} \right\rangle_{f_{n-1}}. \quad (2)$$

Here $\mathcal{Z}(f)$ and $\mathcal{W}_{s_1, s_2}(f)$ the represents general type of partition function (either Z or $Z_M^{(2)}$) and weight at parameter set f . In the realistic simulation, the result of the reweighting is good only if the two parameter points f and f_0 are close enough, i.e., the ratio is closed to 1 [58, 63, 64]. Otherwise, we naturally insert several intermediate points to split the reweighting process,

$$\frac{\mathcal{Z}(f_n)}{\mathcal{Z}(f_0)} = \frac{\mathcal{Z}(f_n)}{\mathcal{Z}(f_{n-1})} \times \dots \times \frac{\mathcal{Z}(f_1)}{\mathcal{Z}(f_0)}, \quad (3)$$

where n is the number of slices. By specifying \mathcal{Z} to $Z_M^{(2)}$ and Z in the above formula, the numerator $Z_M^{(2)}$ and denominator Z^2 in Eq.(1) can be obtained respectively, termed as “bipartite reweight-annealing” algorithm [46]. Moreover, each term of partition function ratio in Eq.(3) can be computed parallelly. On the other hand, to fix the value $\frac{Z_M^{(2)}(f_n)}{Z^2(f_n)}$, a known reference $\frac{Z_M^{(2)}(f_0)}{Z^2(f_0)}$ is required. Usually, we would like anneal to a product state with $\frac{Z_M^{(2)}(f_0)}{Z^2(f_0)} = 1$. Of course, other solvable points are also be used as the reference.

In essential, we intuitively set the incremental process along a real physical parameter path in this algorithm. All the intermediate products are thus the EE values at different parameters points. As a consequence, the efficiency has been greatly improved through taking advantage of the incremental process. This method produces *algebraic multiple EE values* with respect to conventional incremental schemes.

Figure 1(a) displays the flow diagram of our algorithm for simulating Eq.(2) in interacting fermionic systems. Different from normal QMC algorithm, the sampling of the observable

$\langle \frac{\mathcal{W}_{s_1, s_2}(f_n)}{\mathcal{W}_{s_1, s_2}(f_{n-1})} \rangle$ requires two sets of computer memory space for the parameter sets f_n and f_{n-1} . That includes the singular value decomposition (SVD) matrix structure on each time slice, the equal-time Green function and other intermediate variables of the QMC program. Remarkably, they share the *same* copy of the auxiliary field s_1, s_2 , which updates only according to the weight of f_{n-1} . In addition, we keep the weight $\mathcal{W}_{s_1, s_2}(f_n)$ and $\mathcal{W}_{s_1, s_2}(f_{n-1})$ as a global variable to simplify the observable calculation.

Concretely, we initialize the program variables subject to both parameter sets f_{n-1} and f_n without any update regime. In this process, we exactly calculate the initial weight of $\mathcal{W}_{s_1, s_2}(f_n)$ and $\mathcal{W}_{s_1, s_2}(f_{n-1})$ for random auxiliary field s_1, s_2 and keep the weight. We also obtain SVD matrix for both parameter sets, which is used for numerical stability operation and the weight calculation. After initialization, we enter the cycle of update and measurement, indicated as grey dashed box in Fig. 1(a). In each cycle, we first perform a general update step as the origin QMC algorithm for the whole space-time lattice, according to the weight subject to f_{n-1} . In practice, we adopt single-site update, since more simplifications are employed to give a faster computation of the weight and the update ratio. During this process, the updated results marked by red text in Fig. 1(a) are stored. Such results contain the update sequence of the lattice site and whether it is flipped. Subsequently, we update program variables subject to f_n directly according to the stored update results, without any probabilistic criteria. Notice that in this step we use the weight before the update in combination with the update result of f_{n-1} to obtain the updated weight by lower cost, instead of recalculation (see Supplementary Materials (SM) for details). Since both weights subject to f_{n-1} and f_n are already calculated, we conduct a measurement after update process. By repeating this cycle many times, we finally gather the whole measurement data and then take the averaged value as the general Monte Carlo algorithm.

We proceed to discuss the complexity of this algorithm. Once equipped with the above technique, the partition function can be calculated along with the path we chose in the parameters space. Here, a difficulty arises from the calculation of the determinant of the Grover matrix $\det g_{M, s_1, s_2}$. To effectively manage the Grover matrix, we adopt the algorithm in Ref. [53], and always store the g_{M, s_1, s_2}^{-1} in memory for the subsequent operations. Specifically, when applying single site update, the updated inversed Grover matrix is related to the matrix elements before the update. Hence, $O(N_M^2)$ complexity is achieved instead of recalculation with $O(N_M^3)$ complexity in each update step for Grover matrix. Here, N_M is the number of the site in the subregion M . Even if N_M scales linearly with the number of the whole system sites N , the total computation complexity is $O(\beta N^3)$, which also takes account of the complexity of other update process for the auxiliary field. This complexity is on the same scale of the normal QMC algorithm.

Model.— We choose the 2D square lattice Hubbard model

as an example to show the effectiveness of our algorithm. The Hamiltonian is

$$H = -t \sum_{\langle ij \rangle \sigma} (c_{i\sigma}^\dagger c_{j\sigma} + \text{H.c.}) + \frac{U}{2} \sum_i (n_i - 1)^2. \quad (4)$$

$c_{i\sigma}^\dagger, c_{i\sigma}$ are the creation and annihilation operator for single fermion on site i with spin flavor σ , $n_i = \sum_\sigma c_{i\sigma}^\dagger c_{i\sigma}$ represents the total particle number density on site i . t is the hopping strength, and $U > 0$ is the on-site repulsion interaction.

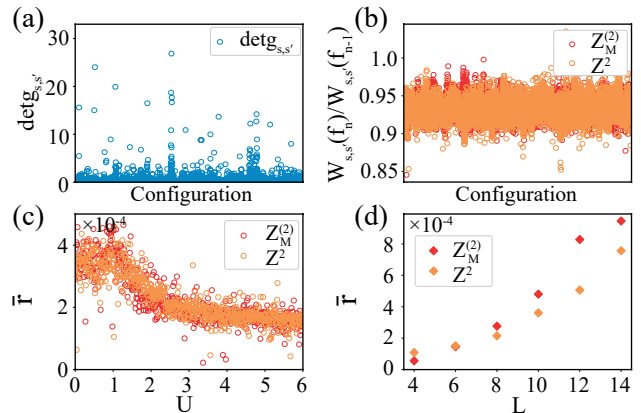


FIG. 2. Comparison in the observable distribution between Grover's methods in (a) and new algorithm in (b). The parameter is chosen as $L = \beta = 4$. $U = 8$ for Grover's method, and the parameter interval $(U, U + \Delta U) = (8, 8.01)$ for the new algorithm. (c) The defined parameter r (ratio between the sample standard deviation and sample mean value) as a function of U . $L = \beta = 4$, and $U \in [0, 6]$. The value of r is at the level of 10^{-4} . r for both two observables has little difference. (d) The averaged r with respect to U (i.e. \bar{r}) as a function of L . Here $\beta = L$. The system size dependence is almost linear.

The QMC algorithm is used to realize the computation of EE parallelly with entangled subregion in Fig. 1(b). Firstly, we make a careful comparison with other existing algorithms to validate the correctness of our algorithms. Note that some parameters of a series of parallel QMC programs are always fixed, such as the Trotter decomposition interval $\Delta\tau$, the projection length β and the system size L . The number of the imaginary time slices which is determined by β and $\Delta\tau$, also maintains as a constant. In practice, we set the model parameter $t = 1$ as an unit, and only vary U as the path in parameter space for EE calculation. A good way to choose the adjacent parameter sets is keeping the ratio between two closest partition functions as a moderate constant, e.g., $\mathcal{Z}(f_n)/\mathcal{Z}(f_{n-1}) \in [0.1, 10]$ (See SM for the discussion on the choice of the intervals). Under this strategy, importance sampling is maintained and segmentation grows algebraically with size.

We first demonstrate the stability and convergence of our algorithm. Previously, the problem for Grover's method [23] comes from the observables, where a few configurations with large values but tiny weights contribute equally to the average value as the most of the configurations. The sampling average

of the minority could be inaccurate when the number of sampling is not enough, as shown in Fig. 4(a). In this sense, it is not an importance sampling, which is a fatal injury for QMC. It is hard to give a proper estimation for the average, since one rarely samples from such configurations.

In our algorithm, such "exceptional" observed values, is converted to the ratio of two exceptional values in the same configurations under adjacent Hamiltonian parameters, according to Eq.(2). We numerically observe that the ratio is no longer deviated from the majority as depicted in Fig. 4(b). Additionally, the distribution of the observables is narrow and no exceptional value appears, indicating high controllability and validity for the errorbar in a single calculation. Moreover, we define one quantity named r in the computation of Z and $Z_M^{(2)}$ to characterize the convergence of the observable, which equals to the ratio between the sample standard deviation and sample mean value. We explore the variance of r against U and L to further investigate the algorithm behavior far from the free fermion limit and in large system, respectively. We find that r varies little with U [Fig. 4(c)]. However, as L increases, the averaged r , named \bar{r} , shows a nearly linear or power law behavior [Fig. 4(d)]. This suggests that more computation cost is required in the large system to promise the same precision as that with small system size, however, it still takes the polynomial time.

To further verify the accuracy of EE results, we compare the obtained EE with other methods in Fig. 4. Firstly, we use the original method proposed by Grover [23] to calculate EE at small system size $L = 4$. Utilizing our method, we observe the consistent result with Grover at various U s in Fig. 4(a). Nonetheless, Grover's method becomes unfaithful at large system size. It is adequate to consider equilibrium algorithm recently proposed by D'Emidio [53] as a benchmark. Here, we refer to the data in Ref. [57] by D'Emidio's method varying the system sizes at the strong interaction limit $U = 8$ in the right panels of Fig. 4(b). The result is in good agreement up to the system size $L = 16$. All the above analyses and comparisons show the high data quality and correctness of the algorithm. Fig. 4 also reveals the advance of our method that, in similar computation time other methods obtain one data point while we gain a data curve. This is a result of the fact that the incremental process of our method is along a real physical parameter path.

EE reveals Fermi surface and Goldstone mode.— To directly uncover the physics behind the Hubbard model, we give a detailed study of EE behavior by scanning the parameter space. To perform a good convergence to the ground state, we exploit the twisted boundary condition (TBC), acting on the choice of the trial wavefunction (See SM for details). As is well-known, the two dimensional square lattice Hubbard model holds a metal-insulator transition. The associate scaling behavior of EE versus the length of subregion in two phases is distinct.

In the absence of U , the model behaves as the metal with square area Fermi surface (FS), whose scaling behavior of EE is dominated by the characteristic leading term of $L \ln L$. The

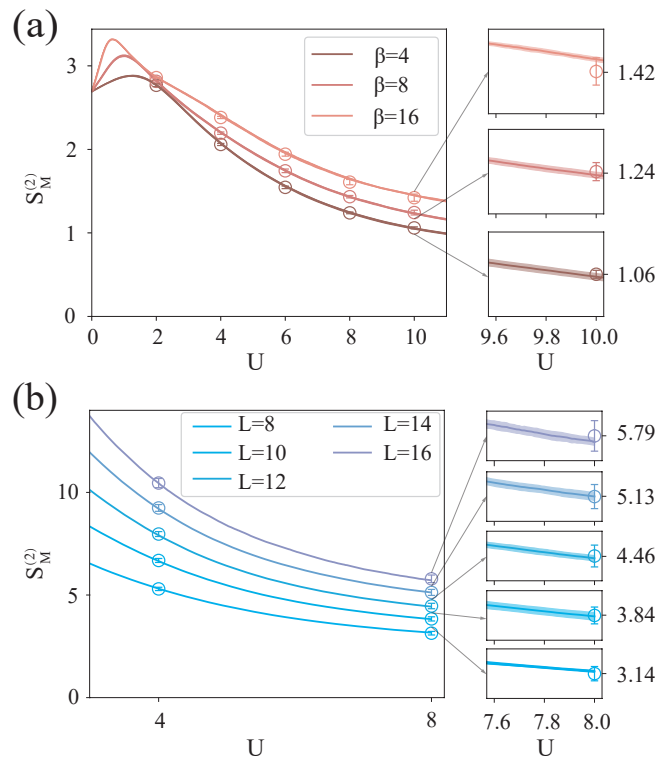


FIG. 3. Comparison in EE results between the new algorithm marked by colored line, and previous methods marked by corresponding colored dots. (a) $S_M^{(2)}$ as a function of U for various projection length β given $L = 4$. The data of red dots comes from Grover's method [23]. The right panels show the zooming at $U \sim 10$ with y -axis range 0.2. (b) $S_M^{(2)}$ as a function of U for various system size L under $L = \beta$. The data of blue dots comes from D'Emidio's method [53], and $U = 8$ data is adapted to Ref. [57]. The right panels show the zooming at $U \sim 8$ with y -axis range 0.6. The shaded errorbar is plotted in the figure, while it is too small to be indicated in the left figure. Note all computations are obtained without TBC.

general form is written as,

$$S_M^{(2)} = AL \ln L + aL + f \ln L + c. \quad (5)$$

The leading term coefficient A is determined by both the shape of the FS and subregion M , expressed by the Widom-Sobelev formula [65, 66].

When adding positive U , the gap gradually opens and the system turns into an insulator. In such a phase, the coefficient A in Eq.(5) vanishes and the associated EE shows an area law. Deep in the insulating phase, the coefficient of the $\ln L$ term b equals to $N_G/2$ under a bipartite cornerless cutting, where the $N_G = 2$ is the number of Goldstone modes in Néel order [67]. In our simulation, the subregion is chosen as the rectangle shape as in Fig. 1(b) to exhibit the Goldstone mode.

We calculate EE up to $L = 16$, constituting the major numerical data of this paper to give an exhibition of EE in Hubbard model. The numerical results of EE show the monotonously decreasing tendency as increasing U , which is valid since the system becomes more insulating. Next, we fit

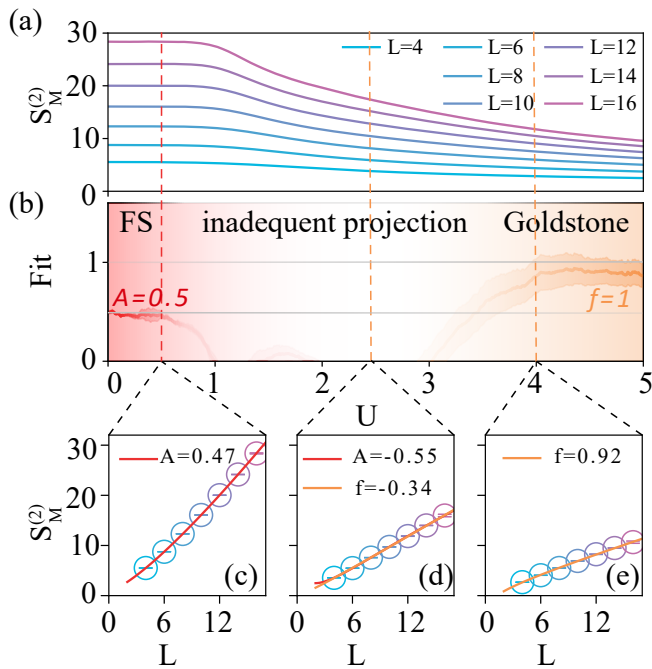


FIG. 4. (a) EE obtained from the new algorithm as a function of U for various L up to 16. Here $\beta = L$ for all curves. (b) Fitting result for the scaling function of EE at various U . At small U , we fits EE with Eq.(5), where the curve of leading term coefficient A is colored by red. At large U , we fits EE with Eq.(5) given $A = 0$, where the curve of universal coefficient f is colored by yellow. The white region represents the intermediate parameter interval, where both function forms are inadequate to give the scaling description. (c) Scaling behavior at $U = 0.5, 2.5$ and 4 . The red and yellow curves are fit results by Eq.(5). Note we use TBC for all computations.

with the function in Eq.(5). The key results of universal coefficients A and f are shown in Fig. 4(b). In addition, we extract three values of U to clearly show the different scaling behavior in Fig. 4(c)-(e). We find at $U \gtrsim 3.5$, the scaling behavior holds consistent with Eq.(5) ($A = 0$, area law), and $f \sim 1$ remains almost unchanged. The deviation of f from 1 attributes to the strong finite size effect of the effective Heisenberg model in the large U limit which has been carefully explained in Ref. [68], and actually it is normal that $f < 1$ in numerical simulations. On the contrary, at $U = 0$ free fermion limit, $L \ln L$ behavior manifests clearly, and fit result of A is close to the 0.5, i.e., analytic solution in the thermodynamic limit [65, 66] (See SM for derivation).

It is found that the goodness-of-fit becomes worse at $U = 2.5$ for both two functions. The reason is the inadequate projection at the small U region, shaded by white in Fig. 4(b), where the gap between the first excitation state and the ground state is small. The problem is intrinsic in PQMC method, which could be improved by choosing proper trial wavefunction or increasing the projection length (See SM for details). Specially, the ground state becomes degenerate at $U = 0$, and the projection fails if the trial wavefunction is the linear combination of the degenerate states. The consequences is multi-

value EE under different trial wavefunctions. We address this issue with TBC, by fixing the rules of the electron wavefunction choice for all system sizes, and EE fits well with Eq.(5) at $U = 0$, as shown in Fig. S2 in SM. Closed to the free fermion limit, we observe a plateau in Fig. 4(a), which is supposed to be a performance sharing the similarity to its trial wavefunction at $U = 0$. Nonetheless, we emphasize the above problem originates from the projection methods itself, rather than the discrepancy of the incremental algorithm.

Summary and outlook.— We report an efficient fermionic QMC algorithm with algebraic acceleration to fix the difficulty of the heavy computational cost of the EE calculation in large-scale interacting fermion systems. By setting the incremental process along the real parameter path, we obtain amounts of EE data in the parameters space upon a single simulation. This is distinguished from the existing methods, where one can get only one data in a single implementation. Our algorithm provides the opportunity to scan EE for exploring its relation against the Hamiltonian parameters. The intrinsic physics in square lattice Hubbard model has been revealed via the EE by our method, such as the FS in $U \rightarrow 0$ limit and Goldstone modes in large U limit. Considering that the highly entangled matter in large-scale and high-dimensional systems plays an essential role in condensed matter and statistic physics, significant efforts has been recently put in developing the numerical methods for spin/boson system, yet the counterpart for fermion systems is rare, even though fermion systems are of great interest in condensed matter. Our methods thus sheds light on the exploration of the intrinsic physics in interacting fermion systems.

Acknowledgment.— We thank the helpful discussion with Wei Zhu, Yao Zhou, Peng Ye, Zi Hong Liu and Xiaofan Luo. This work is supported by National Natural Science Foundation of China (Project No. 12404275 and 12222409), and the fundamental research program of Shanxi province (Project No. 202403021212015). Z.W. and Z.Y. acknowledge the China Postdoctoral Science Foundation under Grants No.2024M752898 and the start-up funding of the Westlake University. G.P. acknowledges the Würzburg-Dresden Cluster of Excellence on Complexity and Topology in Quantum Matter - ct.qmat (EXC 2147, Project No. 390858490). H. S. acknowledges the Royal Society Newton International Fellowship Alumni follow-on funding (AL201024) of UK. The authors thank the high-performance computing center of Westlake University and the Beijing PARATERA Tech Co.,Ltd. for providing HPC resources.

* gaopei.pan@uni-wuerzburg.de

† hengshen@sxu.edu.cn

‡ zhengyan@westlake.edu.cn

- [1] R. Horodecki, P. Horodecki, M. Horodecki, and K. Horodecki, Quantum entanglement, *Rev. Mod. Phys.* **81**, 865 (2009).
- [2] L. Amico, R. Fazio, A. Osterloh, and V. Vedral, Entanglement in many-body systems, *Rev. Mod. Phys.* **80**, 517 (2008).

- [3] N. Laflorencie, Quantum entanglement in condensed matter systems, *Physics Reports* **646**, 1 (2016), quantum entanglement in condensed matter systems.
- [4] B. Zeng, X. Chen, D.-L. Zhou, and X.-G. Wen, [Quantum information meets quantum matter](#) (Springer, 2019).
- [5] H. Casini and M. Huerta, Universal terms for the entanglement entropy in 2+1 dimensions, *Nuclear Physics B* **764**, 183 (2007).
- [6] H. Casini and M. Huerta, Positivity, entanglement entropy, and minimal surfaces, *Journal of High Energy Physics* **2012**, 87 (2012).
- [7] P. Calabrese and A. Lefevre, Entanglement spectrum in one-dimensional systems, *Phys. Rev. A* **78**, 032329 (2008).
- [8] E. Fradkin and J. E. Moore, Entanglement entropy of 2d conformal quantum critical points: Hearing the shape of a quantum drum, *Phys. Rev. Lett.* **97**, 050404 (2006).
- [9] Z. Nussinov and G. Ortiz, Sufficient symmetry conditions for Topological Quantum Order, *Proc. Nat. Acad. Sci.* **106**, 16944 (2009).
- [10] Z. Nussinov and G. Ortiz, A symmetry principle for topological quantum order, *Annals Phys.* **324**, 977 (2009).
- [11] W. Ji and X.-G. Wen, Noninvertible anomalies and mapping-class-group transformation of anomalous partition functions, *Phys. Rev. Research* **1**, 033054 (2019).
- [12] W. Ji and X.-G. Wen, Categorical symmetry and noninvertible anomaly in symmetry-breaking and topological phase transitions, *Phys. Rev. Research* **2**, 033417 (2020).
- [13] L. Kong, T. Lan, X.-G. Wen, Z.-H. Zhang, and H. Zheng, Algebraic higher symmetry and categorical symmetry: A holographic and entanglement view of symmetry, *Phys. Rev. Research* **2**, 043086 (2020).
- [14] X.-C. Wu, W. Ji, and C. Xu, Categorical symmetries at criticality, *Journal of Statistical Mechanics: Theory and Experiment* **2021**, 073101 (2021).
- [15] W. Ding, N. E. Bonesteel, and K. Yang, Block entanglement entropy of ground states with long-range magnetic order, *Phys. Rev. A* **77**, 052109 (2008).
- [16] Q.-C. Tang and W. Zhu, Critical scaling behaviors of entanglement spectra, *Chinese Physics Letters* **37**, 010301 (2020).
- [17] X.-C. Wu, C.-M. Jian, and C. Xu, Universal Features of Higher-Form Symmetries at Phase Transitions, *SciPost Phys.* **11**, 33 (2021).
- [18] G. Vidal, J. I. Latorre, E. Rico, and A. Kitaev, Entanglement in quantum critical phenomena, *Phys. Rev. Lett.* **90**, 227902 (2003).
- [19] P. Calabrese and J. Cardy, Entanglement entropy and quantum field theory, *Journal of Statistical Mechanics: Theory and Experiment* **2004**, P06002 (2004).
- [20] J. Eisert, M. Cramer, and M. B. Plenio, Colloquium: Area laws for the entanglement entropy, *Reviews of Modern Physics* **82**, 277 (2010).
- [21] M. B. Hastings, I. González, A. B. Kallin, and R. G. Melko, Measuring renyi entanglement entropy in quantum monte carlo simulations, *Phys. Rev. Lett.* **104**, 157201 (2010).
- [22] S. Humeniuk and T. Roscilde, Quantum monte carlo calculation of entanglement renyi entropies for generic quantum systems, *Phys. Rev. B* **86**, 235116 (2012).
- [23] T. Grover, Entanglement of interacting fermions in quantum monte carlo calculations, *Phys. Rev. Lett.* **111**, 130402 (2013).
- [24] J. Zhao, Z. Yan, M. Cheng, and Z. Y. Meng, Higher-form symmetry breaking at ising transitions, *Phys. Rev. Research* **3**, 033024 (2021).
- [25] J. Zhao, Y.-C. Wang, Z. Yan, M. Cheng, and Z. Y. Meng, Scaling of entanglement entropy at deconfined quantum criticality, *Phys. Rev. Lett.* **128**, 010601 (2022).
- [26] B.-B. Chen, H.-H. Tu, Z. Y. Meng, and M. Cheng, Topological disorder parameter: A many-body invariant to characterize gapped quantum phases, *Phys. Rev. B* **106**, 094415 (2022).
- [27] Y.-C. Wang, N. Ma, M. Cheng, and Z. Y. Meng, Scaling of the disorder operator at deconfined quantum criticality, *SciPost Phys.* **13**, 123 (2022).
- [28] Y.-C. Wang, M. Cheng, and Z. Y. Meng, Scaling of the disorder operator at $(2+1)d$ u(1) quantum criticality, *Phys. Rev. B* **104**, L081109 (2021).
- [29] W. Jiang, B.-B. Chen, Z. H. Liu, J. Rong, F. F. Assaad, M. Cheng, K. Sun, and Z. Y. Meng, Many versus one: The disorder operator and entanglement entropy in fermionic quantum matter, *SciPost Phys.* **15**, 082 (2023).
- [30] Z. Yan and Z. Y. Meng, Unlocking the general relationship between energy and entanglement spectra via the wormhole effect, *Nature Communications* **14**, 2360 (2023).
- [31] J. Zhao, B.-B. Chen, Y.-C. Wang, Z. Yan, M. Cheng, and Z. Y. Meng, Measuring renyi entanglement entropy with high efficiency and precision in quantum monte carlo simulations, *npj Quantum Materials* **7**, 69 (2022).
- [32] Y. D. Liao, G. Pan, W. Jiang, Y. Qi, and Z. Y. Meng, The teaching from entanglement: 2d su(2) antiferromagnet to valence bond solid deconfined quantum critical points are not conformal, arXiv e-prints (2023), [arXiv:2302.11742 \[cond-mat.str-el\]](#).
- [33] Z. H. Liu, Y. Da Liao, G. Pan, M. Song, J. Zhao, W. Jiang, C.-M. Jian, Y.-Z. You, F. F. Assaad, Z. Y. Meng, and C. Xu, Disorder operator and renyi entanglement entropy of symmetric mass generation, *Phys. Rev. Lett.* **132**, 156503 (2024).
- [34] J. I. Latorre, E. Rico, and G. Vidal, Ground state entanglement in quantum spin chains, *Quant. Inf. Comput.* **4**, 48 (2004).
- [35] O. Legeza and J. Sólyom, Two-site entropy and quantum phase transitions in low-dimensional models, *Phys. Rev. Lett.* **96**, 116401 (2006).
- [36] W.-L. Chan and S.-J. Gu, Entanglement and quantum phase transition in the asymmetric hubbard chain: Density-matrix renormalization group calculations, *Journal of Physics Condensed Matter* **20** (2008).
- [37] J. Ren, X. Xu, L. Gu, and J. Li, Quantum information analysis of quantum phase transitions in a one-dimensional V_1 - V_2 hard-core-boson model, *Phys. Rev. A* **86**, 064301 (2012).
- [38] Z. Liu, R.-Z. Huang, Y.-C. Wang, Z. Yan, and D.-X. Yao, Measuring the boundary gapless state and criticality via disorder operator, *Phys. Rev. Lett.* **132**, 206502 (2024).
- [39] P. Laurell, A. Scheie, C. J. Mukherjee, M. M. Koza, M. Enderle, Z. Tylczynski, S. Okamoto, R. Coldea, D. A. Tennant, and G. Alvarez, Quantifying and controlling entanglement in the quantum magnet Cs_2CoCl_4 , *Phys. Rev. Lett.* **127**, 037201 (2021).
- [40] H. Li and F. D. M. Haldane, Entanglement spectrum as a generalization of entanglement entropy: Identification of topological order in non-abelian fractional quantum hall effect states, *Phys. Rev. Lett.* **101**, 010504 (2008).
- [41] D. Poilblanc, Entanglement spectra of quantum heisenberg ladders, *Phys. Rev. Lett.* **105**, 077202 (2010).
- [42] S. Wu, X. Ran, B. Yin, Q.-F. Li, B.-B. Mao, Y.-C. Wang, and Z. Yan, Classical model emerges in quantum entanglement: Quantum monte carlo study for an ising-heisenberg bilayer, *Phys. Rev. B* **107**, 155121 (2023).
- [43] Z. Liu, R.-Z. Huang, Z. Yan, and D.-X. Yao, Demonstrating the wormhole mechanism of the entanglement spectrum via a perturbed boundary, *Phys. Rev. B* **109**, 094416 (2024).
- [44] M. Song, J. Zhao, Z. Yan, and Z. Y. Meng, Different temperature dependence for the edge and bulk of the entanglement

- hamiltonian, *Phys. Rev. B* **108**, 075114 (2023).
- [45] D. J. Luitz, X. Plat, N. Laflorencie, and F. Alet, Improving entanglement and thermodynamic rényi entropy measurements in quantum monte carlo, *Phys. Rev. B* **90**, 125105 (2014).
- [46] Z. Wang, Z. Wang, Y.-M. Ding, B.-B. Mao, and Z. Yan, Bipartite reweight-annealing algorithm to extract large-scale data of entanglement entropy and its derivative in high precision, arXiv e-prints (2024), [arXiv:2406.05324 \[cond-mat.str-el\]](https://arxiv.org/abs/2406.05324).
- [47] B.-B. Mao, Y.-M. Ding, and Z. Yan, Sampling reduced density matrix to extract fine levels of entanglement spectrum, [arXiv:2310.16709 \[cond-mat.str-el\]](https://arxiv.org/abs/2310.16709).
- [48] C. Li, R.-Z. Huang, Y.-M. Ding, Z. Y. Meng, Y.-C. Wang, and Z. Yan, Relevant long-range interaction of the entanglement hamiltonian emerges from a short-range gapped system, *Phys. Rev. B* **109**, 195169 (2024).
- [49] Y.-M. Ding, Y. Tang, Z. Wang, Z. Wang, B.-B. Mao, and Z. Yan, Tracking the variation of entanglement rényi negativity : an efficient quantum monte carlo method, arXiv e-prints (2024), [arXiv:2409.10273 \[cond-mat.str-el\]](https://arxiv.org/abs/2409.10273).
- [50] M. Song, J. Zhao, M. Cheng, C. Xu, M. M. Scherer, L. Janssen, and Z. Y. Meng, Deconfined quantum criticality lost, [arXiv:2307.02547 \[cond-mat.str-el\]](https://arxiv.org/abs/2307.02547).
- [51] Z. Deng, L. Liu, W. Guo, and H. qing Lin, Diagnosing $so(5)$ symmetry and first-order transition in the $j - q_3$ model via entanglement entropy, [arXiv:2401.12838 \[cond-mat.str-el\]](https://arxiv.org/abs/2401.12838).
- [52] J. D’Emidio, Entanglement entropy from nonequilibrium work, *Phys. Rev. Lett.* **124**, 110602 (2020).
- [53] J. D’Emidio, R. Orús, N. Laflorencie, and F. de Juan, Universal features of entanglement entropy in the honeycomb hubbard model, *Phys. Rev. Lett.* **132**, 076502 (2024).
- [54] X. Zhou, Z. Y. Meng, Y. Qi, and Y. Da Liao, Incremental swap operator for entanglement entropy: Application for exponential observables in quantum monte carlo simulation, *Phys. Rev. B* **109**, 165106 (2024).
- [55] X. Zhang, G. Pan, B.-B. Chen, K. Sun, and Z. Y. Meng, Integral algorithm of exponential observables for interacting fermions in quantum monte carlo simulations, *Phys. Rev. B* **109**, 205147 (2024).
- [56] Y. D. Liao, Controllable incremental algorithm for entanglement entropy in quantum monte carlo simulations, arXiv e-prints (2023), [arXiv:2307.10602 \[cond-mat.str-el\]](https://arxiv.org/abs/2307.10602).
- [57] G. Pan, Y. Da Liao, W. Jiang, J. D’Emidio, Y. Qi, and Z. Y. Meng, Stable computation of entanglement entropy for two-dimensional interacting fermion systems, *Phys. Rev. B* **108**, L081123 (2023).
- [58] Y.-M. Ding, J.-S. Sun, N. Ma, G. Pan, C. Cheng, and Z. Yan, Reweight-annealing method for calculating the value of partition function via quantum monte carlo, arXiv e-prints (2024), [arXiv:2403.08642 \[cond-mat.str-el\]](https://arxiv.org/abs/2403.08642).
- [59] S. R. White, D. J. Scalapino, R. L. Sugar, E. Y. Loh, J. E. Gubernatis, and R. T. Scalettar, Numerical study of the two-dimensional hubbard model, *Phys. Rev. B* **40**, 506 (1989).
- [60] S. G and K. S., E, Auxiliary field monte-carlo for quantum many-body ground states, *Annals of Physics* **168**, 1 (1986).
- [61] Z^2 is the square of the partition function of the whole system, where in practice one could only simulate Z and then square.
- [62] J. D’Emidio, Entanglement entropy from nonequilibrium work, *Phys. Rev. Lett.* **124**, 110602 (2020).
- [63] Z. Dai and X. Y. Xu, Residual entropy from temperature incremental monte carlo method, arXiv e-prints (2024), [arXiv:2402.17827 \[cond-mat.str-el\]](https://arxiv.org/abs/2402.17827).
- [64] R. M. Neal, Annealed importance sampling, *Statistics and computing* **11**, 125 (2001).
- [65] D. Gioev and I. Klich, Entanglement entropy of fermions in any dimension and the widom conjecture, *Phys. Rev. Lett.* **96**, 100503 (2006).
- [66] H. Leschke, A. V. Sobolev, and W. Spitzer, Scaling of rényi entanglement entropies of the free fermi-gas ground state: A rigorous proof, *Phys. Rev. Lett.* **112**, 160403 (2014).
- [67] M. A. Metlitski and T. Grover, Entanglement Entropy of Systems with Spontaneously Broken Continuous Symmetry, arXiv e-prints (2011), [arXiv:1112.5166 \[cond-mat.str-el\]](https://arxiv.org/abs/1112.5166).
- [68] Z. Deng, L. Liu, W. Guo, and H. Lin, Improved scaling of the entanglement entropy of quantum antiferromagnetic heisenberg systems, *Physical Review B* **108**, 125144 (2023).
- [69] B. Swingle, Entanglement entropy and the fermi surface, *Phys. Rev. Lett.* **105**, 050502 (2010).

Supplemental Material

Fast update procedure

Here, we provide detailed description of the fast update procedure. In QMC, the calculation of partition function follows,

$$Z = \langle \Psi_T | e^{-2\beta H} | \Psi_T \rangle = C^m \sum_s \det [P^\dagger B_s(2\beta, 0)P]. \quad (\text{S1})$$

And the weight is expressed as,

$$W_s = C^m \det [P^\dagger B_s(2\beta, 0)P], \quad (\text{S2})$$

where $|\Psi_T\rangle$ is the trial wavefunction, whose information is encoded in matrix P . B matrix is determined by the Hamiltonian. Note C^m is omitted in the simulation, because the observables is the ratio of two partition functions, defined as $\langle \frac{W_{s_1, s_2}(f_n)}{W_{s_1, s_2}(f_{n-1})} \rangle$ in the main text. The simplest way to obtain weight after the update $W_{s'}$ is recalculating Eq.(S2), which needs SVD matrix and cost $O(N^3)$ complexity. In practice, we adopt single site update, where Sherman-Morrison methods reduce the complexity to $O(N^2)$ by calculating the update ratio $R = \frac{\det[P^\dagger B_{s'}(2\beta, 0)P]}{\det[P^\dagger B_s(2\beta, 0)P]}$. In addition, considering the observables is more complex than original QMC, one operation is design to always keep W_s in the memory space for the observable calculation. That requires only one exact calculation of W_s at the beginning, and then repeated update W_s to $W_{s'}$ using the calculated ratio R . Then the total complexity remains $O(\beta N^3)$, in the same order as the original QMC. In a word, the fast update process naturally offers to update for the observables, in which case we call this algorithm "passing the weight".

Such an idea can be also realized in the presence of $\det g_{s_1, s_2}$ in the weight. We have,

$$Z_M^{(2)} = \sum_{s_1, s_2} W_{M, s_1, s_2} = \sum_s W_{M, s}, \quad (\text{S3})$$

$$W_{M, s} = W_s W_{s'} \det g_{M, s_1, s_2},$$

where the weight $W_{M, s}$ contains two parts, the former is identical to the weight W_s , and the latter is the determinant of the Grover matrix. In the single site update regime, we use methods proposed by D'Emidio (See Ref.[53] for details), saving g_{M, s_1, s_2}^{-1} for calculation. Then the complexity for calculating the ratio $R = \frac{\det g_M^{s'_1, s'_2}}{\det g_M^{s_1, s_2}}$ (or $R = \frac{\det g_M^{s_1, s'_2}}{\det g_M^{s_1, s_2}}$) scales with $O(N_M^2)$, which equals to $O(N^2)$, in our case $N_M = N/2$. Such process could avoid recalculating the determinant at each measurement to obtain the ratio. Therefore, the total complexity is still controlled in $O(\beta N^3)$.

Unfortunately, the above method could be problematic due to the passing process. We calculated the exact value of the determinant before and after the single update process and compared it with the ratio. We numerically find the simplified computing method for Grover matrix ratio R may sometimes not be exact. Such inaccuracy could be a negligible effect on the update process, since it only slightly change the update probability. However, the inaccurate R has relatively serious influence on the observable calculations, i.e. the updated weight $W_{M, s'}$ obtained by $W_{M, s}$ and R . What is even worse, the error could accumulate and result in completely incorrect results.

To avoid this, we recalculate the determinant at the end of each sweep of space-time sites and conduct it as the exact value of the weight, which contains $\frac{\beta N}{\Delta\tau}$ single updates. The process is similar to the numerical stabilization in auxiliary field QMC. We numerically find the error between recalculation and passing weight process are smaller than 10^{-4} , in which case, the calculated EE is in accordance with the results from the previous method within the errorbar (See Fig.2 in the main text). One can speculate the frequency for doing stabilization depends on the number of the updates, namely, large system size and β require more stabilizations. Under such condition, the operation should be adjusted according to the parameters to control the passing error.

Twisted boundary condition

In the initialization process, we use twisted boundary condition (TBC) to implement various choices of trial wavefunctions for QMC program. In general, we expects the choice of trial wavefunction to be as close as possible to the ground state wavefunction, in which condition the associated projection length can be small. Generally speaking, to construct the initial wavefunction, we diagonalize the free fermion Hamiltonian in the momentum space, then find several electron wavefunctions

with the lowest eigen-energies satisfying the half-filling condition. In fact, on the calculation of lattice model, such ground state wavefunction could not be unity. The problems come from the momentum points on the FS, which lead to the degeneracy of the ground state. Considering the simplest case, $L = 4$ square lattice free fermion model with nearest-neighbor hopping, the FS is of skew square shape, with six k-points on it, depicted in Fig. S1(a). The half-filling condition demands five electronic eigenstates with negative energies and an additional three on the FS. Therefore, the amount of choice, i.e. degeneracy, for $L = 4$ case is 20 (400 for two spin species), which gets larger along with the system size. In each calculation, we only select one of such degenerate eigenstates to form the P matrix in QMC. However, we numerically find the choice of the trial wavefunction varies with the compile environment. Importantly, these 20 eigenstates have different EEs, not to mention the linear combination of these orthogonal eigenstates. The former analysis leads to multi-values of EE in the free limit without TBC in different machine, which seems quite awkward, but in fact an existing problem.

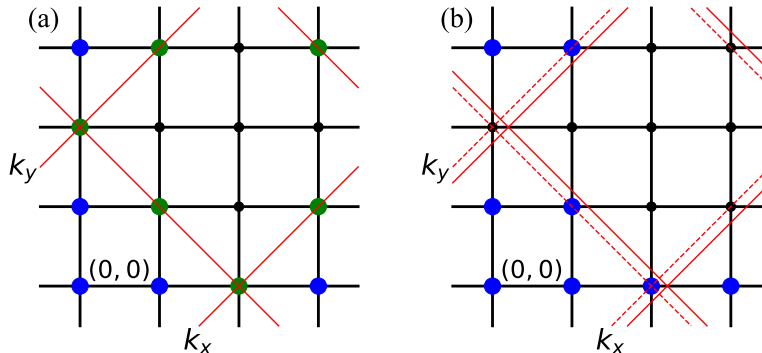


FIG. S1. Sketch map of TBC in the momentum space for $L = 4$. (a) In presence of TBC, the FS goes through six momentum points, colored by green. The five blue dots are the momentum points with negative energies. (b) When $\phi_x \neq 0$, the FS translates along the x -direction, drawn by the solid line after the translation. Eight momentum points possessing negative energies are colored in blue, which is exactly half of the total number.

An optional way to avoid the multi-choice problem dependent on non-physical factors is to adopt the TBC before diagonalization. The TBC is applied by adding Peries phase factor on each hopping amplitude as Eq.(S4). Such condition translates the eigenstates along the direction TBC added in the momentum space. We use ϕ to control the translation degree. On the two dimensional square lattice, we add different ϕ along x and y direction, and the Hamiltonian with TBC writes,

$$H = -t \sum_{i\sigma} \left(e^{i\phi_x} c_{i\sigma}^\dagger c_{i+\hat{x}\sigma} + e^{i\phi_y} c_{i\sigma}^\dagger c_{i+\hat{y}\sigma} + \text{H.c.} \right). \quad (\text{S4})$$

As an example, we only add a small x -direction twist, i.e., $\phi_y = 0, \phi_x = 0.00001$, and show the FS after translation in Fig. S1(b). There are exact eight negative eigenvalues marked by blue, just half of the total number of momentum points. Therefore, this kind of TBC leads to the half-filling condition, which adapts to all even system size. We calculate EE at $L = 4 - 16$ under such condition, and fit by Eq. (5) in the main text, shown in Fig. S2. We numerically find A is close to its thermodynamic limit value 0.5.

One could notice that since the entangled region M is unequal for x and y direction, applying y -direction twist $\phi_x = 0, \phi_y = 0.00001$ of course results in different EE values. Fortunately, we also obtain similar fitting results for $L \ln L$ term coefficient in Fig. S2. We conclude that, if the TBC is fixed for all system sizes, or more generally the choice principle of half-filled electron eigenvectors in momentum space, the leading term coefficient of EE could emerge close to the thermodynamic limit. Therefore, even though the ground state EE is not unique in QMC, we are able to identify the scaling behavior for further analysis.

Projection length

An intrinsic principle of the projection QMC is acting on $\exp(-\Delta\tau H)$ on the imaginary time ceaselessly to eliminate the weight of excitation state, where the projection length β controls the degree of ground state proximity. Such process will become difficult to handle when the gap between the ground state and the first excitation tends to zero, since quite large β is needed to reach the exact ground state. It is still acceptable if the gap is algebraically small, However, for Hubbard model at small U limit it is exponentially small which will cause a problem. Indeed, the condition applies to the square lattice Hubbard model near

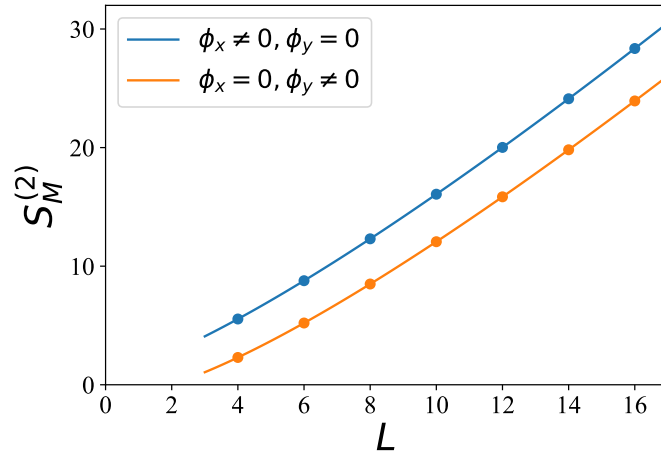


FIG. S2. Fitting results of free fermion EE under different TBCs. The blue and yellow line represents the TBC along x and y direction, respectively. We fit two data sets with Eq. (5) in the main text and focus on the leading term coefficient A . Here, $A_x = 0.48(3)$, $A_y = 0.51(3)$ for the TBC along x and y direction. Both values are close to the thermodynamic limit value 0.5. For $\phi \neq 0$ condition, we give ϕ a small but non-zero value, e.g. 0.00001 in the program.

$U = 0$, where the gap diverge as $\sim e^{-\beta\sqrt{\frac{t}{U}}}$. Therefore, the calculation at small U region may be unfaithful. As a result, the previous study for EE is carried deep in the insulating phase, i.e., large U limit, to get the favourable fitting result[57]. Except for β and U , the trial wavefunction also bears on the how well the projection performance (See TBC section for details). Therefore, the projection length β , serving as a tuning parameter, is adjusted to large enough to reach the ground state as close as possible for various choice of trial wavefunction and U s.

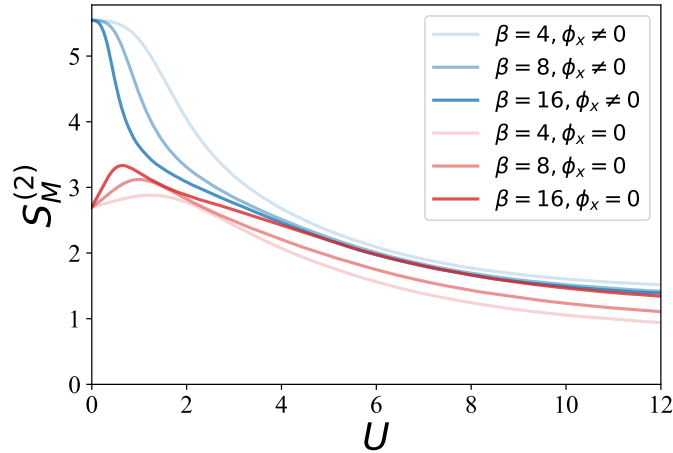


FIG. S3. EE results from various projection length and trial wave function at $L = 4$. The choice of trial wavefunction is controlled by the TBC, colored by blue (no TBC) and red ($\phi_x = 0.00001$). The gradation of color reflects the projection length. At $U = 0$, the distinct TBC leads different EE values. As U becomes large, various curves converge. The two curves with darkest color are most closed to each other, indicating that at large U , $\beta = 16$ is enough to expose the value of ground state EE.

In Fig. S3, we compute EE with various projection lengths and different TBC conditions. At $U = 0$, the EE is different with or without TBC. Besides, the projection operation does not influence the results. At small U , where projection makes a difference, leading to all different EEs. This indicates that the projection length is inadequate, under which condition the wavefunction after projection differs a lot from the ground state. Nevertheless, we find at large U , EE data with same β but different trial wavefunctions gradually coincide as β increases. The two curves with the darkest color show results of $\beta = 16$, which are close to each other, expressing that such projection length is large enough to generate ground state properties regardless of the trial wavefunction.

Ground state wavefunction

To further explore the projection issue, we offer a simple perturbation theory for Hubbard model defined on lattice. Here, we focus on the small U region and treat U as a perturbation. Taking $L = 4$ as an example, on the half-filling condition, the ground state of free fermion limit have degeneracy due to multi-choice for filling at the FS, shown in Fig. S1. There are total 400 degenerate states, which constitute a subspace for 2^{32} -dimension of total Hilbert space. Then we numerically solve the eigenvalue and the eigenvector in this subspace at the presence of U , and find a non-degenerate ground state. To write down the explicit form of ground state wavefunction, we choose the particle number basis, $|\uparrow_1 \uparrow_2 \cdots \uparrow_6 \downarrow_1 \downarrow_2 \cdots \downarrow_6\rangle$, where $1, 2, \cdots, 6$ represents six momentum points on the FS, and \uparrow, \downarrow are spin up and down index. At each momentum points with one spin flavor, the fermion can occupy or not, expressed as 0 or 1. We do the perturbation at small U and obtain the wavefunction, written as,

$$|\psi_g\rangle = \frac{1}{\sqrt{20}} \sum_P P(\uparrow) \otimes \bar{P}(\downarrow), \quad (\text{S5})$$

where P represents state where three of six momentum points to occupy one particle for each, for example $|100110\rangle$, and \bar{P} is opposite configuration, e.g. $|011001\rangle$. There are total 20 choice for the combinations, and $|\psi_g\rangle$ is the equal-weight superposition state of 20 basis wavefunctions. We note $|\psi_g\rangle$ also satisfies the exchange invariance for spin up and down. However, we emphasize the form is unable to be written as the trial wavefunction or P matrix in QMC, since the wavefunction should be the direct product of the electron wavefunctions of two spins. In real simulation, we could only use other forms of trial wavefunction. For example, we use the TBC to choose certain wavefunction, and then do the projection operation to reach the ground state. Thus it is always hard to get ground state EE at small U by QMC if the gap is small.

Convergence and optimization for ΔU

In this section, we aim to investigate the optimization by tuning the control parameter in the new algorithm. As above, one of the most important parameter, which also serves as the essence of an algorithm, is ΔU , expressed in the example of Hubbard model. Considering that ΔU is always small, it is the reason why we regard the method as the new incremental algorithm in parameter space. If ΔU is large, the algorithm returns back to the analogue of Grover's original method, which is also in face of the exceptional values problem. However, much dense U values may be waste of resources. If one is only attracted to the behavior of one point in parameter space, for example the behavior near QCP, the possible way to avoid waste, on the premise of the correctness of the algorithm is by setting unfixed ΔU along the whole track in the parameter space, or calculating EE at certain parameters near the QCP by means of other methods. However, considering the case, when the consecutive behavior of EE in parameter space raises one's interest, one could only make use of the former way to give a proper division of ΔU . To simplify the study, we consider the ΔU as a constant for whole path, but serves as a tuning parameter to optimize the new algorithm.

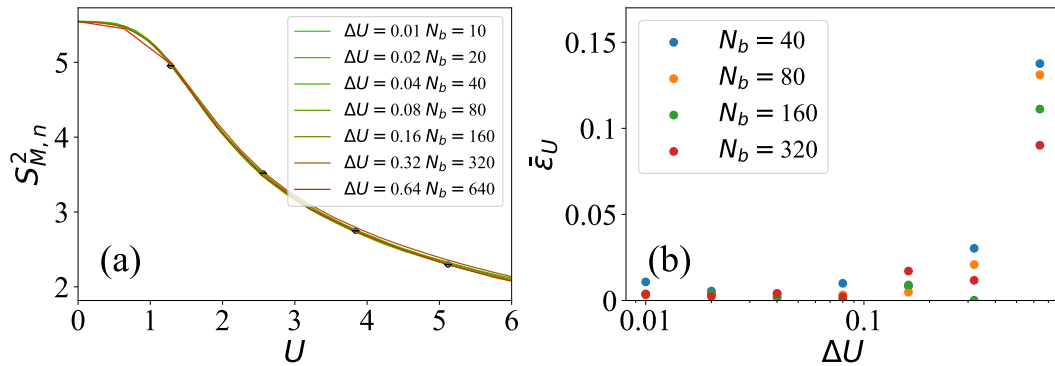


FIG. S4. (a) EE results of new algorithm $S_{M,n}^{(2)}$ for various ΔU at $L = 4, \beta = 4$. The color change from green to red, corresponding the increasement of ΔU . The black dots are calculated using Grover's method at $U = 1.28, 2.56, 3.84, 5.12$. For justice, we also increase N_b to prove the usage of same computation resource. We observe that the red curves has large deviation from the Grover's result. All the simulations are done in presence of TBC. (b) ϵ versus ΔU and N_b at $L = 4, \beta = 4$. As we expect, the deviation decreases as the interval becomes small, or the measurement becomes large. The deviation is smaller than 10^{-3} when we choose Δ smaller than 0.1, and basically remain unchanged if we continue reducing ΔU , indicating our proper choice for ΔU in the computation of the paper. Note there are 200 sweeps in each bin for the smallest ΔU . The number of the sweep is linearly proportion to ΔU .

Firstly, we check for the validity for EE results by varying ΔU . Taking the calculation from $U = 0$ to 6 as example, supposed we have the same computing resources, when increasing ΔU , it is fair to enhance the number of samples correspondingly. In Fig. S4(a), we show the results from different ΔU and compare with the results from Grover[?]. At small ΔU , we observe a good consistency between the new algorithm and the Grover's method. As ΔU increase, the EE curves gradually deviate from the data points by Grover's method, raising the challenge for the data correctness. Besides, we add the number of bins, named N_b for each ΔU calculations to study the convergence to Grover's result.

To give a quantitative description, we define the deviation, named ϵ , between the results from two methods at certain U points. $\epsilon = |S_{M,n}^{(2)} - S_{M,g}^{(2)}|/S_{M,g}^{(2)}$, where $S_{M,n}^{(2)}$ and $S_{M,g}^{(2)}$ represents the EE results from the new algorithm and Grover's method, respectively. We do enough measurement to prove the accuracy for Grover's method, since it serves as the benchmark data. We further define $\bar{\epsilon}$ to describe the average deviation for many U points.

We plot the value of $\bar{\epsilon}$, as a function of ΔU and N_b , shown in Fig. S4(b). As we expect, $\bar{\epsilon}$ gradually converges to 0 as ΔU decrease. In comparison to ΔU , increasing N_b only has small influence on the deviation. Such quantitative study shows the deviation depends more on ΔU , instead of N_b . Above findings inspires us to reduce ΔU to exploit the advantages for the incremental method. And the value we choose for ΔU is refer to such analysis, where the deviation is small enough to reach convergence.

Possible promotion of the new algorithm efficiency for incremental methods

In the section, we provide an quantitatively analysis for the degree of the efficiency promotion by dividing the parameter interval. We emphasize that the analysis is only valid on condition that the exception value problem is not serious, in other words, ΔU is small enough. Suppose $\mathcal{Z}(f)/\mathcal{Z}(f_0) = 1/y$, where y is much bigger than 1. If one divides $[f_0, f]$ into n subintervals, and requires each $\mathcal{Z}(\beta_{k-1})/\mathcal{Z}(\beta_k) \approx \epsilon$, then one has $\epsilon \approx (1/y)^{1/n}$. The corresponding Monte Carlo steps before and after the division scale with $\mathcal{O}(y^2)$ and $\mathcal{O}(n/\epsilon^2) = \mathcal{O}(ny^{2/n})$, respectively. For example, if $y = 10^{10}$ as the general order for EE on the lattice model, a crudely calculation needs $\mathcal{O}(10^{20})$ MC steps. If one has only $n = 10$ subintervals, the number of the MC steps just decreases to only $\mathcal{O}(10^3)$. Therefore, the incremental methods could in principle reach exponential magnitude of the increase of algorithm efficiency.

Widom-Sobolev equation for free fermion limit

The scaling behavior of ground state EE in free fermion system have experienced a long study, where the pioneer work was concluded as Widom conjecture[65]. The crucial discovery is that in presence of the FS, the leading term of EE scales as $L^{d-1} \ln L$, where d is the dimension exceeding the general area law behavior. Latter, Brian proposed a phenomenological analysis for the emergence of $L \ln L$ term[69]. In brief, for two dimensional system, each point on the FS owns a chiral model contributing to the $\ln L$ term, as described by one dimensional conformal field theory. Since the mode density scale with L , EE with FS scales as $L \ln L$. Besides, the leading term coefficient also depends on the shape of FS and subregion. In 2014, Leschke gave a rigorous proof of this, known as the Widom-Sobolev equation[66]. The n -order Renyi entropy has

$$S_M^{(n)} \sim \frac{n+1}{24n} \frac{L^{d-1} \ln L}{(2\pi)^{d-1}} \int_{\partial\Omega} \int_{\partial\Gamma} |\mathbf{n}_x \cdot \mathbf{n}_p| \mathbf{d}S_x \mathbf{d}S_p, \quad (S6)$$

where $\partial\Omega, \partial\Gamma$ represents the integral along the boundary of the subregion M and FS. $\mathbf{n}_x, \mathbf{n}_p$ is the unit normal vector with respect to the subregion and FS in the momentum space. $\mathbf{d}S_x$ integrates in the real space with unit length, $\mathbf{d}S_p$ in the momentum space. Note the subregion is chose as a rectangle, shown in Fig. 1(b) in the main text, where the boundaries only exist along verticle direction due to the period boundary condition. Since the boundary for subregion and FS are all straight, the term $|\mathbf{n}_x \cdot \mathbf{n}_p|$ can be regarded as the projection for two boundaries from $\mathbf{d}S_x$ and $\mathbf{d}S_p$. Therefore, the total integral is divided into the single integral of each boundary,

$$\begin{aligned} S_M^{(n)} &\sim \frac{n+1}{24n} \frac{L^{d-1} \ln L}{(2\pi)^{d-1}} \int_{\partial\Omega} \int_{\partial\Gamma} \mathbf{d}S_x \mathbf{d}S_p \cos(\beta_{x,p}), \\ &\sim \frac{n+1}{24n} \frac{L^{d-1} \ln L}{(2\pi)^{d-1}} \int_{1,2} \int_{a,b,c,d} \mathbf{d}S_x \mathbf{d}S_p \cos(\beta_{x,p}) \end{aligned} \quad (S7)$$

$\beta_{x,p}$ represents the angle between two boundaries 1, 2, a, b, c, d are boundaries of subregion and FS, respectively. The result of the integral is 8π . Note we have two spin species in the free fermion limit, the final coefficient of A in Eq. (5) is 0.5 for theoretical result.

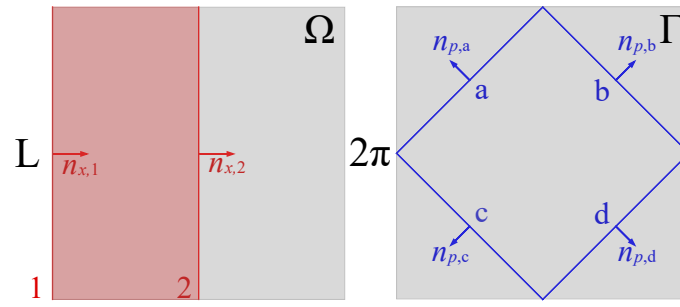


FIG. S5. The sketch map of boundaries of real space subregion in the left panel, and FS in the momentum space. The real space boundary is divided into two parts, labeled 1 and 2, where $n_{x,1}$ and $n_{x,2}$ are the associated normal vectors. The FS boundary is divided into four parts, labeled a, b, c, d , where $n_{x,a}, n_{x,b}, n_{x,c}, n_{x,d}$ are the associated normal vectors.